

# Learning Priors for Non Rigid SfM from Casual Videos

Yoni Kasten<sup>1</sup>, Wuyue Lu<sup>2</sup>, and Haggai Maron<sup>1,3</sup>

<sup>1</sup> NVIDIA Research

<sup>2</sup> Simon Fraser University

<sup>3</sup> Technion

**Abstract.** We tackle the long-standing challenge of reconstructing 3D structures and camera positions from videos. The problem is particularly hard when objects are transformed in a non-rigid way. Current approaches to this problem make unrealistic assumptions or require a long optimization time. We present TRACKSTO4D, a novel deep learning-based approach that enables inferring 3D structure and camera positions from dynamic content originating from in-the-wild videos using a single feed-forward pass on a sparse point track matrix. To achieve this, we leverage recent advances in 2D point tracking and design an equivariant neural architecture tailored for directly processing 2D point tracks by leveraging their symmetries. TRACKSTO4D is trained on a dataset of in-the-wild videos utilizing only the 2D point tracks extracted from the videos, without any 3D supervision. Our experiments demonstrate that TRACKSTO4D generalizes well to unseen videos of unseen semantic categories at inference time, producing equivalent results to state-of-the-art methods while significantly reducing the runtime compared to other baselines. Project page: <https://tracks-to-4d.github.io>.

**Keywords:** Structure From Motion · Dynamic Videos · 3D Reconstruction · Equivariance · Symmetries

## 1 Introduction

Predicting 3D structures in dynamic scenes is a challenging problem. In contrast to rigid scenes where the epipolar geometry constraints hold between the corresponding points of different views [17], determining the depth of a moving point from monocular views is an ill-posed problem. Moreover, while multiview camera pose estimation can be solved successfully by Structure from Motion methods [30, 37, 53], these techniques tend to fail in scenarios with significant non-rigid motion [21].

*Background and previous work.* Unfortunately, current approaches to solving this problem are based on unrealistic assumptions or suffer from long optimization times per scene that make them inapplicable to real-world problems. More

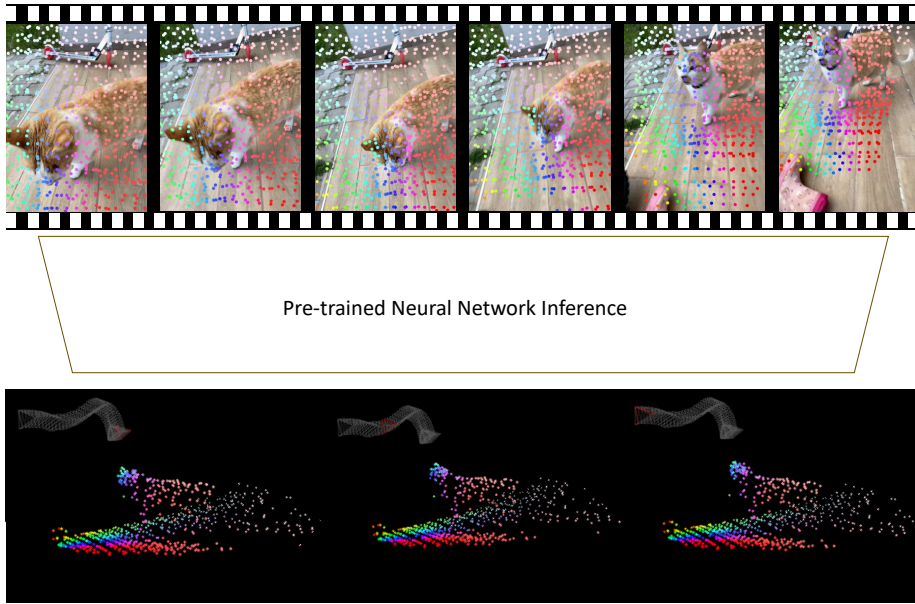


**Fig. 1:** We present TRACKSTO4D, a method for mapping a set of 2D point tracks extracted from casual dynamic videos into their corresponding 3D locations and camera motion. At inference time, our network predicts the non-rigid structure and camera motion in a single feed-forward pass. **Top.** An example showing the input video frames ordered from left to right. A set of pre-extracted point tracks that are used as input to our network and presented in corresponding colors. **Bottom.** The outputs of our network for 3 time steps as observed from the right side of the scene. The camera trajectory is present as gray frustums, whereas the current camera is marked in red. The reconstructed 3D scene points are presented in corresponding colors to the input tracks on the top. See video visualizations [here](#).

concretely, early techniques for Non-Rigid SFM [6] used matrix factorization of long-term point tracks matrix of the non-rigid scene part. This was done by assuming that a small linear basis and per-frame coefficients can formulate the dynamic structure. By further assuming an orthographic camera is used, they omitted camera translations and solved for rotations and 3D structure by matrix factorization. While follow-up work improved accuracies [11, 22], this setup is still not practical for real-world casual videos, captured by pinhole cameras. Recently, the Neural Radiance Field (NeRF) [28] concept has brought major progress to novel view synthesis and surface reconstruction [49, 60] for static scenes. While some follow-up work extended NeRF to non-rigid scenes [23, 24, 33], optimizing a non-rigid NeRF requires a long, and per-scene optimization. Other recent approaches [21, 26, 62, 63] optimized for consistent depth maps given a specific monocular video by fine-tuning pre-trained single-view-depth-predictions [34]. These methods showed impressive progress in camera and non-rigid structure estimation, but also require per-video optimization at inference time. Other ap-

proaches learned prior and parameterizations for specific non-rigid object classes such as humans [25,36]. This prior enables shorter inference times for obtaining 3D structures from monocular videos that contain instances from the learned category [55]. However, this approach does not generalize well across shape categories and mostly requires per-video finetuning.

*Our approach.* In this work, we propose TRACKSTO4D, a novel deep learning-based approach for predicting the 3D dynamic Non-Rigid Structure And camera Motion from videos. Our key observation is that the 2D motion present in casual videos shares common patterns across a variety of semantic video categories. Crucially, and as was suggested by [6], this motion can be effectively encoded into a point track matrix, where each entry represents the 2D position of a tracked point in a specific video frame. Rather than processing image pixels or semantic features that vary dramatically across different scenes and objects, we propose directly processing these point track matrices to learn generic, class-agnostic features. This also differs from the common approach of using optical flow representations of motion, as utilizing optical flow fields as input to deep neural networks is non-trivial.

TRACKSTO4D builds on the recent progress in point tracking [12,18], which introduced the ability to extract long-term point tracks from casual videos. We leverage this progress and design a deep neural network architecture, that maps the point tracks of a given video into corresponding camera poses, 3D points, and per-point non-rigid motion level values (See Fig. 1). Crucially, the mapping we aim to learn preserves two natural symmetries: (1) the points being tracked can be arbitrarily permuted without affecting the problem; (2) the frames containing these points exhibit temporal structure, adhering to an approximate time-translation symmetry. Following the Geometric Deep Learning paradigm [7], we build upon recent theoretical advances in equivariant learning [27] and integrate these two symmetries into our network architecture using dedicated attention mechanisms.

Predicting the camera poses and the 3D non-rigid motion from 2D motion alone is an ill-posed problem without any constraints, and equivalent to finding the 3D structure from each frame [3]. Inspired by previous work [6], we model the predicted 3D point cloud as a weighted sum of a 3D structure basis, where the first basis is assumed to fully represent the rigid points, and the rest of the basis elements are used to complete the non-rigid deviation for the non-rigid points. The predicted motion level values determine the non-rigidity of each 3D world point, i.e. the inconsistency of the rigid assumption that is represented by the first basis element for this world point.

In our experiments, TRACKSTO4D is trained on the Common Pets dataset [38] using only 2D point tracks extracted by [18], without any 3D supervision by simply minimizing the reprojection errors. Interestingly, we observe that by just "watching" point tracks in videos, our network learns to infer their 3D location and the camera motion. We evaluate our method on test data with GT depth maps and demonstrate that it generalizes well, and produces comparable results to the state-of-the-art methods, with significantly shorter inference time.

*Contributions.* In summary, our contributions are: (1) Designing an equivariant network architecture that maps from 2D point trajectories into corresponding non-rigid structures and camera poses; (2) Introducing a training paradigm to identify the rigid part of the scene for constraining the camera poses; (3) Simple training on casual videos without any 3D supervision; (4) Demonstrating fast inference time, accurate results, and strong generalization across animal categories.

## 2 Related Work

*Structure from Motion* The Structure from Motion (SfM) problem recovers the 3D structure and the camera poses from images. Early methods [39,44] factorized a 2D measurement matrix of corresponding image points into a multiplication of a camera poses matrix by a 3D points matrix. These methods assume that each recovered 3D point is tracked over the entire image sequence which is not the case in practical use cases. Incremental approaches for SfM [1,37,53] start from a minimal set of images, to build an initial reconstruction. Then, the rest of the images are added to the scene one by one, by finding 2D correspondences from the new image into scene points. To prevent drift, Bundle Adjustment [45] is repeatedly applied to the reconstruction during this process. Several global methods [10,19,32,51,52] reduced the running time by using relative two-view geometries between image pairs to extract absolute camera poses in a single step, followed by a final round of Bundle Adjustment.

Recently, Moran et al. [29] presented a method for applying an order equivariant architecture for mapping a set of multiview image correspondences into two sets of cameras and 3D points. It was trained on a dataset of scenes and obtained a reduced optimization time on novel scenes, due to the learned prior. A follow-up work [8] improved generalization by adding graph attention layers into the architecture of Moran et al. Other recent deep learning-based techniques used differentiable Bundle Adjustment layers [40,47], or diffusion models [48,61]. The above-mentioned techniques assumed that the structure is rigid such that the whole scene can be represented in a single 3D structure.

*Simultaneous Localization and Mapping (SLAM)* In contrast to SfM which assumes unordered images, monocular Simultaneous Localization and Mapping (SLAM) methods [15,30,31] get as input a sequence of video frames recorded by a single camera. These methods often define a set of keyframes for reconstructing the scene with a mapping thread, while registering every new frame into the structure by a localization thread. The mapping thread repeatedly applies Bundle Adjustment for updating the structure. ORB-SLAM [30] uses feature points for mapping a sparse scene representation and tracks the camera with sparse point matches. Other methods [14,15,31] use denser scene representations and align cameras directly by using photometric constraints.

More recent methods combine classical approaches with deep learning-based tools e.g. depth prediction from a single image, optical flow prediction, or relative

camera pose estimation [5, 41, 50, 59, 65, 66]. As in SfM, these methods assume rigid scenes, fail to produce the cameras in scenes with large portions of non-rigid motion, and cannot reproduce non-rigid parts of the scene. DROID-SLAM [43] used synthetic data with ground truth 3D supervision for learning to predict camera poses via deep-based bundle adjustment on keyframes while excluding dynamic objects. ParticleSfM [64] pre-trained a motion prediction network on a synthetic dataset with ground truth supervision, and used it to filter out any non-rigid content for reproducing the cameras in dynamic scenes. Both, [43, 64] do not infer the non-rigid 3D structure.

*Test-Time Optimization for Non-Rigid Scenes* Recent methods [21, 26, 62, 63] finetuned the monocular depth estimation from a pre-trained model [34, 35] using optical flow constraints [42], for obtaining consistent dense depth maps for a monocular video. [62] further optimized motion maps that represent the  $\gamma$  parameters of zero mean Cauchy distributions for handling scenes with large dynamic motion. [16, 54] use depth from single image estimations, to improve novel view synthesis in dynamic scenes. [24] further optimized for the unknown camera poses together with the dynamic radiance field optimization. LASR [56], ViSER [57] and BANMo [58] optimize for a dynamic surface given a monocular video by assuming rigid bones and linear blend skinning weights. However, all the above-mentioned methods require per-scene optimization, resulting in slow inference. Recently, [38] presented the Common Pets in 3D (COP3D) dataset that contains casual, in-the-wild videos of pets, and used it to learn priors for novel view synthesis in dynamic scenes.

### 3 Problem formulation

Our problem setup is illustrated in Fig. 2. Given a video of  $N$  frames, let  $M \in \mathbb{R}^{N \times P \times 3}$  be a pre-extracted point tracks tensor (Fig. 2, left side). This tensor represents the two-dimensional information about a set of  $P$  world points that are tracked throughout the video. Each element in the tensor,  $M_{i,j}$ , stores three values:  $(x, y, o)$  where  $x, y \in \mathbb{R}$  are respectively the observed horizontal and vertical locations of point  $j$  in frame  $i$ , and  $o \in \{0, 1\}$  indicates whether point  $j$  is observed in frame  $i$  or not. Our goal is to learn a function  $f$  to map the input point tracks tensor  $M$  into a set of per-frame camera poses  $\{R_i, \mathbf{t}_i\}_{i=1}^N$  and per-frame 3D points  $\{X_i\}_{i=1}^N$ , where  $R_i \in SO(3)$ ,  $\mathbf{t}_i \in \mathbb{R}^3$ ,  $X_i \in \mathbb{R}^{P \times 3}$  (Fig. 2, right side).

*Discussion.* We note that given enough point tracks,  $M$  contains the 2D motion constraints that can be provided by the video. The source of each 2D motion constraint can be either from a global camera 3D motion or from an independent object motion. While the pixel appearance and semantic information could be used as well as inputs in our task, we find that the 2D motion signal  $M$  gives useful geometric constraints for our setup. Moreover, this abstraction of the video helps our network generalize well to out-of-distribution videos with object

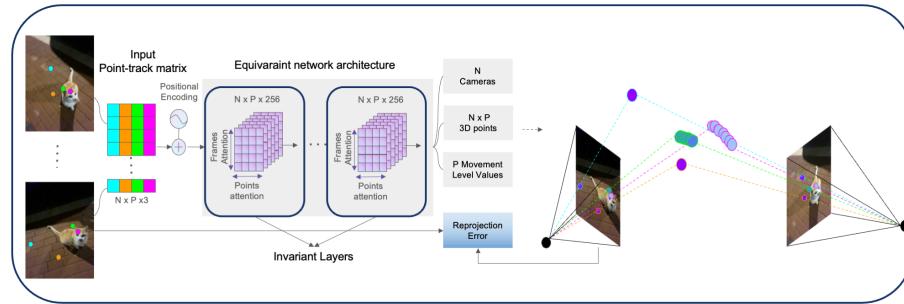


**Fig. 2: Our pipeline** Our network takes as input a set of 2D point tracks (left) and uses several multi-head attention layers while alternating between the time dimension and the track dimension (middle). The network predicts cameras, per-frame 3D points, and per-world point movement value (right). The 3D point colors illustrate the movement level values, such that points with high/low motion values are presented in blue/purple colors respectively. These outputs are used to reproject the predicted points into the frames for calculating the reprojection error losses. See details in the text.

classes that have not been observed during training but share similar 2D motion characteristics as we show in our experiments. Therefore  $f$  only uses  $M$  as input and does not rely on the input video once  $M$  has been extracted.

## 4 Method

### 4.1 Overview

Our pipeline is illustrated in Fig. 2. Our method receives  $M \in \mathbb{R}^{N \times P \times 3}$  as input. This tensor is being processed by a neural architecture composed of multi-head attention layers where the attention is calculated sequentially on the  $P$  and the  $N$  dimensions in each layer (Sec. 4.3). After several such layers, we perform a projection to  $N$  per-frame parameters and  $P$  per-world-point parameters which determine the camera poses and 3D dynamic structure (Sec. 4.2). This projection is done by first pooling over the secondary dimension and applying suitable layers to each one of the outputs to get the per-camera and per-world points parameters respectively. Our network is trained by minimizing the reprojection error and other regularization losses (Sec. 4.4) that are used to update the model parameters.

### 4.2 Constraining the Non-Rigid Structure and Motion

Given the input 2D tracks, we wish to describe their motion by global camera motion and non-rigid self-motion. The 2D motion that is produced from rigid points constrains well the camera motion, but predicting the camera poses and

the 3D non-rigid motion from 2D motion alone is an ill-posed problem without any constraints [3].

We tackle this challenge in two ways. First, as done in classical Non-Rigid Structure from Motion [6], we constrain the output points to be formulated by a linear combination of basis elements. This constrains the 3D motion to be simple and prevents "jumps" in the unconstrained depth. More formally we assume that the non-rigid structure is formulated by a few basis elements  $B_1, \dots, B_K \in \mathbb{R}^{P \times 3}$  such that  $X_i = \sum_{k=1}^K c_{ik} B_k$  where  $\{c_{ik}\}_{k=1}^K$  are the  $K$  coefficients which define the 3D structure of frame  $i$ .

Secondly, we define the first basis element  $B_1 \in \mathbb{R}^{P \times 3}$  to be a rigid approximation of the points, such that the first basis coefficient in every frame is 1, i.e.  $c_{i1} = 1$  for  $i = 1, \dots, N$ . This helps in constraining the camera motion from the 2D motion of the rigid scene part. However, since this global rigid approximation cannot explain the 2D motion that is produced by the non-rigid world points, we model the reprojection error of the rigid approximation with  $P$  zero-mean Cauchy distributions. For a non-rigid world point,  $B_1$  by itself cannot produce low reprojection errors, and therefore its associated  $\gamma$  is expected to be higher. The parameters of the Cauchy distributions,  $\gamma_1, \dots, \gamma_P \in \mathbb{R}_+$  (Fig. 2, "Movement Level Values") are predicted as well by the network and our training maximizes the likelihood of this assumption (see details in Sec. 4.4). This allows our network to benefit from the rigid part for camera pose prediction while still being robust to the non-rigid motion. The rest of the basis elements determine the non-rigid deviation of the non-rigid points from the rigid approximation.

In summary, our function  $f$  gets  $M \in \mathbb{R}^{N \times P \times 3}$  as an input and predicts per-frame outputs:

$$R_i \in SO(3), \mathbf{t}_i \in \mathbb{R}^3, \{c_{ik}\}_{k=2}^K, \text{ for } i = 1, \dots, N \quad (1)$$

and per-point outputs:

$$B_1, \dots, B_K \in \mathbb{R}^{P \times 3}, \gamma_1, \dots, \gamma_P \in \mathbb{R}_+ \quad (2)$$

which together define the non-rigid structure and motion.

### 4.3 Architecture

Following the geometric deep learning paradigm, our goal is to design a neural architecture that respects the underlying symmetries and structure of the data.

*Symmetry analysis.* Our input is a tensor  $M \in \mathbb{R}^{N \times P \times 3}$  representing a sequence of  $N$  frames each with  $P$  point coordinates. This structure gives rise to two key symmetries: First, the order of the  $P$  points within each frame does not matter - permuting this axis results in an equivalent problem [27]. Formally, this axis has a permutation symmetry  $S_P$  where  $S_P$  is the symmetric group on  $P$  elements. Second, along the temporal  $N$  axis, we have an approximate translation symmetry arising from the ordered video sequence. This means that translating the time frames is required to result in nearly the same overall representation. We

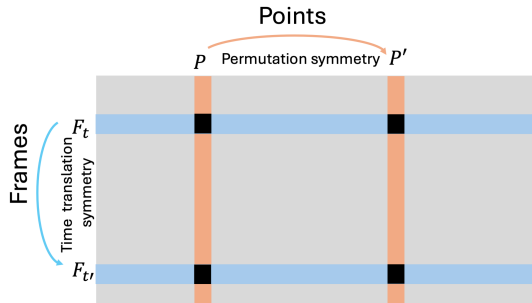


**Fig. 3:** The symmetry structure of our problem. Frames (vertical) have time translation symmetry while points (horizontal) have set permutation symmetry.

model this with a cyclic group  $C_N$  of order  $N$ . Both symmetries are illustrated in Fig. 3.

Taken together, the full symmetry group of the input space is the direct product  $\mathcal{G} = C_N \times S_P$  combining these frame and point permutation symmetries<sup>4</sup>. Next, we will design an architecture equivariant to  $\mathcal{G}$ , so that we can incorporate these domain priors and ensure that the model takes into account the underlying data structure.

*Network Architecture.* Building on the analysis from the Deep Sets for Symmetric elements (DSS) approach [27], if we assumed we can use only linear layers, our architecture would take the form:

$$F(M)_{:,j} = L_1(M_{:,j}) + \sum_{j'=1}^P L_2(M_{:,j'}) \quad (3)$$

where  $L$  is a translation equivariant function,  $M_{:,j} \in \mathbb{R}^{N \times d}$  are the columns of  $M$  representing all the inputs for a specific tracked point,  $F(M)_{:,j} \in \mathbb{R}^{N \times d'}$  is the output column and we have  $d, d'$  input and output feature channels respectively. While valid, this linear layer design might not be the optimal choice. To enhance the model, we incorporate additional nonlinear layers that are well-suited for sequence and set structures data. One particularly effective choice is the transformer layer [46]. Importantly, by leveraging attention mechanisms and temporal positional encodings, the transformer processes sequential input while respecting its ordering and context. Specifically, our layer  $F$  is formulated very similarly to Equation (3) and is implemented by replacing the convolutions ( $L_i$ ) and summations in Equation (3) with two self-attention mechanisms and suitable temporal positional encoding across the  $N$  dimension. We provide more architecture and implementation details in the supplementary.

<sup>4</sup> This is different from the symmetry group studied in [29], where the temporal structure was not exploited



#### 4.4 Training

Given a dataset of point track representations:  $\{M_1, \dots, M_L\}$ , our method trains the function  $f$  to minimize the loss function over all elements in the dataset:

$$f = \operatorname{argmin}_f \frac{1}{L} \sum_{i=1}^L \mathcal{L}(M_i, f) \quad (4)$$

Our loss function is defined by:

$$\mathcal{L} = \lambda_{\text{Reproject}} \mathcal{L}_{\text{Reproject}} + \lambda_{\text{Rigid}} \mathcal{L}_{\text{Rigid}} + \lambda_{\text{Negative}} \mathcal{L}_{\text{Negative}} + \lambda_{\text{Sparse}} \mathcal{L}_{\text{Sparse}} \quad (5)$$

The first loss is the reprojection error given by the structure and the cameras predicted by  $f$ :

$$\mathcal{L}_{\text{Reproject}} = \frac{1}{\sum_{i=1}^N \sum_{j=1}^P M_{ij}^o} \sum_{i=1}^N \sum_{j=1}^P M_{ij}^o \mathcal{R}(X_{ij}, R_i, \mathbf{t}_i, M_{ij}^{xy}) \quad (6)$$

where  $\mathcal{R}(X_{ij}, R_i, \mathbf{t}_i, M_{ij}^{xy})$  is the reprojection error when projecting the point  $X_{ij}$  with the camera pose  $(R_i, \mathbf{t}_i)$  with respect to the measured point  $M_{ij}^{xy}$ :

$$\mathcal{R}(X_{ij}, R_i, \mathbf{t}_i, M_{ij}^{xy}) = \left\| \begin{pmatrix} (R_i^T(\mathbf{X}_{ij} - \mathbf{t}_i))_{1,2} \\ (R_i^T(\mathbf{X}_{ij} - \mathbf{t}_i))_3 \end{pmatrix} - M_{ij}^{xy} \right\| \quad (7)$$

As discussed in Sec. 4.2, the first predicted basis element  $B_1 \in \mathbb{R}^{P \times 3}$  defines a rigid (fixed in time) approximation. Our network also predicts a movement coefficient  $\gamma_j$  for each world point that defines a zero-mean Cauchy distribution. Given  $\gamma_j$  and the reprojection error  $r_{ij} = \mathcal{R}(B_{1j}, R_i, \mathbf{t}_i, M_{ij}^{xy})$  of the  $j^{\text{th}}$  point of  $B_1$  that is projected by the  $i^{\text{th}}$  camera, the negative log-likelihood of  $r_{ij}$  distributed according to the  $\gamma_j$ -zero-mean Cauchy distribution is proportional to:

$$\mathcal{C}(r_{ij}, \gamma_j) = \log \left( \gamma_j + \frac{r_{ij}^2}{\gamma_j} \right) \quad (8)$$

Our rigid loss calculates the mean negative log-likelihood over all observed points in all frames:

$$\mathcal{L}_{\text{Rigid}} = \frac{1}{\sum_{i=1}^N \sum_{j=1}^P M_{ij}^o} \sum_{i=1}^N \sum_{j=1}^P M_{ij}^o \mathcal{C}(\mathcal{R}(B_{1j}, R_i, \mathbf{t}_i, M_{ij}^{xy}), \gamma_j) \quad (9)$$

As in [29] we regularize the points to be in front of the camera by:

$$\mathcal{L}_{\text{Negative}} = - \sum_{i=1}^N \sum_{j=1}^P M_{ij}^o \operatorname{Min}(R_i^T(\mathbf{X}_{ij} - \mathbf{t}_i)_3, 0) \quad (10)$$

	ATE ↓ (mm)	RPE Trans ↓ (mm)	RPE Rot ↓ (deg)	Inference ↓ Time
DROID-SLAM [43]	5.08	3.60	0.20	10 seconds
ParticleSfM [64]	12.79	6.95	0.51	11 minutes
RCVD [21]	43.95	25.77	2.31	20 minutes
CasualSAM [62]	6.90	3.95	0.22	130 minutes
Ours (cats only)	8.96	3.79	0.23	<b>0.16(+8.6)</b> seconds
Ours (cats only)+BA	4.22	2.86	<b>0.17</b>	0.4(+8.6) seconds
Ours (dogs only)	8.03	3.54	0.23	<b>0.16(+8.6)</b> seconds
Ours (dogs only)+BA	<b>4.19</b>	<b>2.83</b>	<b>0.17</b>	0.4(+8.6) seconds
Ours (dogs+cats)	8.11	3.68	0.24	<b>0.16(+8.6)</b> seconds
Ours (dogs+cats)+BA	4.21	2.86	<b>0.17</b>	0.4(+8.6) seconds

**Table 1: Camera Poses Accuracy.** Quantitative comparisons between our method to previous methods for camera accuracy and running time. For our method, we compare three versions of (1) training only on cats, (2) training only on dogs, and (3) training on both. We evaluate all methods on an unseen test set of cats and dogs. We further show our accuracies after one round of Bundle Adjustment. For our method’s running time, we also mention the point tracks extraction time in parenthesis (+8.6 seconds) which is performed by [18] as a preprocess.

We further find it beneficial to regularize the deviation from the rigid approximation  $B_1$  to be sparse at locations with low  $\gamma$  values:

$$\mathcal{L}_{\text{Sparse}} = \frac{1}{P(K-1)} \sum_{k=2}^K \sum_{j=1}^P \frac{1}{3\gamma_j} (|B_{kj1}| + |B_{kj2}| + |B_{kj3}|) \quad (11)$$

where  $\gamma$  is detached from the gradient calculation for this loss.

## 5 Experiments

### 5.1 Training Details

We trained our network on the cat and dog partitions from the COP3D dataset [38], which contains a diverse set of casual real-world videos of pets. We trained our network from scratch three times to test our generalization capability between semantic categories: once on the cat partition, once on the dog partition, and once on both partitions combined. In total, we used 733 cat videos and 753 dog videos for training. We trained our networks for 7000 and 3500 epochs for the single-class and multi-class setups respectively. Training our method lasts about one week on a single Tesla V100 GPU with 32GB memory. We used the Adam optimizer [20] with a learning rate of  $10^{-4}$ . For our non-rigid bases  $B_1, \dots, B_K$  (Sec. 4.2) we used  $K = 12$ . Our method assumes known camera internal parameters which are provided by the dataset and used to normalize the point tracks as a preprocess.

	Abs Rel ↓		$\delta < 1.25 \uparrow$		$\delta < 1.25^2 \uparrow$		$\delta < 1.25^3 \uparrow$	
	Dynamic	All	Dynamic	All	Dynamic	All	Dynamic	All
RCVD [21]	0.40	3.6e+7	0.43	0.72	0.75	0.90	0.92	0.96
MiDaS [4]	0.16	6.1e+4	0.78	0.71	0.97	0.88	1.00	0.93
CasualSAM [62]	<b>0.09</b>	<b>0.06</b>	<b>0.93</b>	<b>0.97</b>	<b>0.99</b>	<b>0.99</b>	<b>1.00</b>	<b>1.00</b>
Our (cats only)	0.11	0.08	0.88	0.92	<b>0.99</b>	0.98	<b>1.00</b>	<b>1.00</b>
Our (dogs only)	0.12	0.08	0.85	0.91	<b>0.99</b>	<b>0.99</b>	<b>1.00</b>	<b>1.00</b>
Our (dogs+cats)	0.12	0.08	0.85	0.91	0.98	0.98	<b>1.00</b>	<b>1.00</b>

**Table 2: Depth Accuracy** We show a comparison to previous methods on the predicted depth for the trajectories compared to their GT depths. We compare three instances of our method, each trained on a different partition of the dataset.

	Abs Rel ↓		$\delta < 1.25 \uparrow$		$\delta < 1.25^2 \uparrow$		$\delta < 1.25^3 \uparrow$		Rep.(pix.) ↓		ATE ↓	RPE Trans ↓	RPE Rot ↓
	Dyn.	All	Dyn.	All	Dyn.	All	Dyn.	All	Dyn.	All	(mm)	(mm)	(deg)
Set of Sets	0.27	0.15	0.60	0.77	0.87	0.94	0.97	0.99	9.86	5.33	16.87	5.53	0.39
No $\mathcal{L}_{\text{Rigid}}$	0.77	0.36	0.25	0.46	0.48	0.70	0.68	0.82	1.00	0.86	96.20	29.86	0.99
No $\gamma$	0.22	0.16	0.66	0.73	0.93	0.91	0.99	0.97	4.54	2.41	13.91	4.86	0.29
K=30	0.14	0.09	0.81	0.90	0.97	0.98	0.99	0.99	4.88	2.78	9.39	3.68	0.23
K=2	0.11	0.08	0.88	0.91	0.98	0.98	1.00	1.00	8.58	3.56	9.31	3.86	0.25
DSS	1.65	0.58	0.19	0.35	0.34	0.60	0.47	0.74	63.75	70.60	34.90	22.63	1.64
No $\mathcal{L}_{\text{Sparse}}$	0.17	0.13	0.79	0.80	0.95	0.94	1.00	0.99	4.57	2.73	11.79	7.99	0.55
Full	0.11	0.08	0.88	0.92	0.99	0.98	1.00	1.00	3.98	1.97	8.96	3.79	0.23

**Table 3: Ablation Study.** We evaluate the contribution of different parts from our method by changing one property each time. See details in the text.

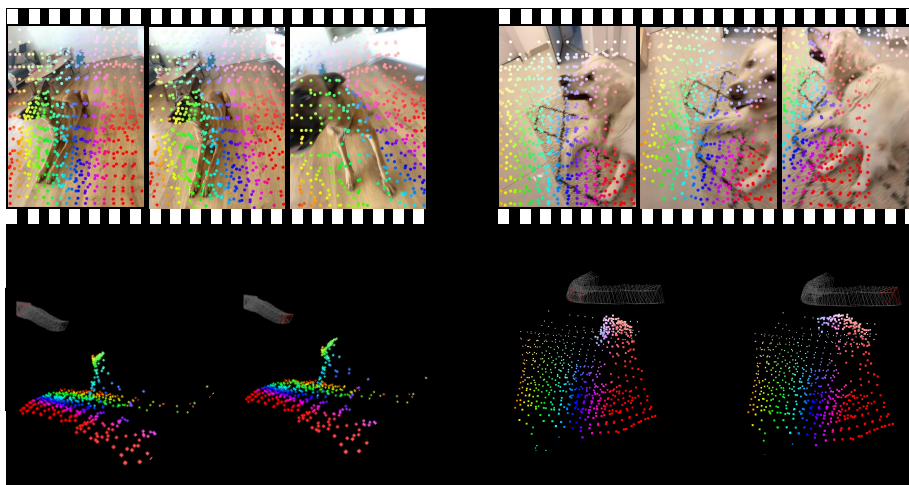


**Fig. 4: Qualitative Results.** We present qualitative results in the same format as in Fig. 1. **Top.** 3 frames from 2 different test video sequences with point tracks marked with corresponding colors. **Bottom.** A 3D visualization of the outputs of our method, from two time stamps. As the scene is observed from the same viewpoint in each pair, a non-rigid movement can be observed.

## 5.2 Evaluation Data

While the COP3D dataset provides cameras that were extracted by COLMAP [37], we note that the non-rigid structure was captured as well in part of their reconstruction which indicates that its reconstruction might not be accurate. Furthermore, the coordinates system units of these reconstructions are unknown. Finally, this dataset does not have any depth map information for evaluating the non-rigid structure.

For evaluation, we used an RGBD sensor and collected 21 casual videos of dogs and cats, each with 50 frames. The depth maps were used as ground truth for evaluating the reconstructed structure. We extracted the cameras by running COLMAP on the images while masking out the pet areas with dilated masks provided by [68]. The cameras were scaled to millimeter units using the provided GT depth. We verified that this data includes enough non-rigid motion, by also including several videos that COLMAP failed to reconstruct without the masks. We further verified manually that the camera trajectories look reasonable. Note that this is test data that our network did not see during training and was not used to tune our hyperparameters.

## 5.3 Results

We evaluated our method on the test data. Qualitative visualizations are presented in Fig. 1 and Fig. 4. We also show a visualization of the movement level values,  $\gamma$  in Fig. 5. We compared our method to the state-of-the-art methods and evaluated both, the camera poses and the structure. The camera poses were evaluated using the Absolute Translation Error (ATE), the Relative Translation Error (RTE), and the Relative Rotation Error (RRE) metrics after coordinates system alignment. The results are presented in Tab. 1. We compare three training possibilities of our method of training only on cats, only on dogs, and on both. As can be seen in the table, the results are similar in all 3 cases, even though the test set contains samples of both dogs and cats. This shows that our network generalizes well to unseen animal classes. Our output camera poses as inferred by the network are already accurate and outperform some of the prior methods. We further show the results of our method after a single and short round of Bundle Adjustment, which makes our method the most accurate one.

Tab. 1 also compares the running times between the methods. It can be seen that our method, even with bundle adjustment is the fastest one when most of the time (8.6 seconds) is used to extract the input point tracks with [18].

To evaluate the structure we compare our method using depth evaluation metrics [13]. The results are presented in Tab. 2, and show that our inferred structure is comparable to the state-of-the-art [62] while taking significantly shorter running times (a few seconds for our method versus more than two hours for [62]). We also note that in contrast to other methods in the table, we are not using any supervision from a depth-from-single-image network.

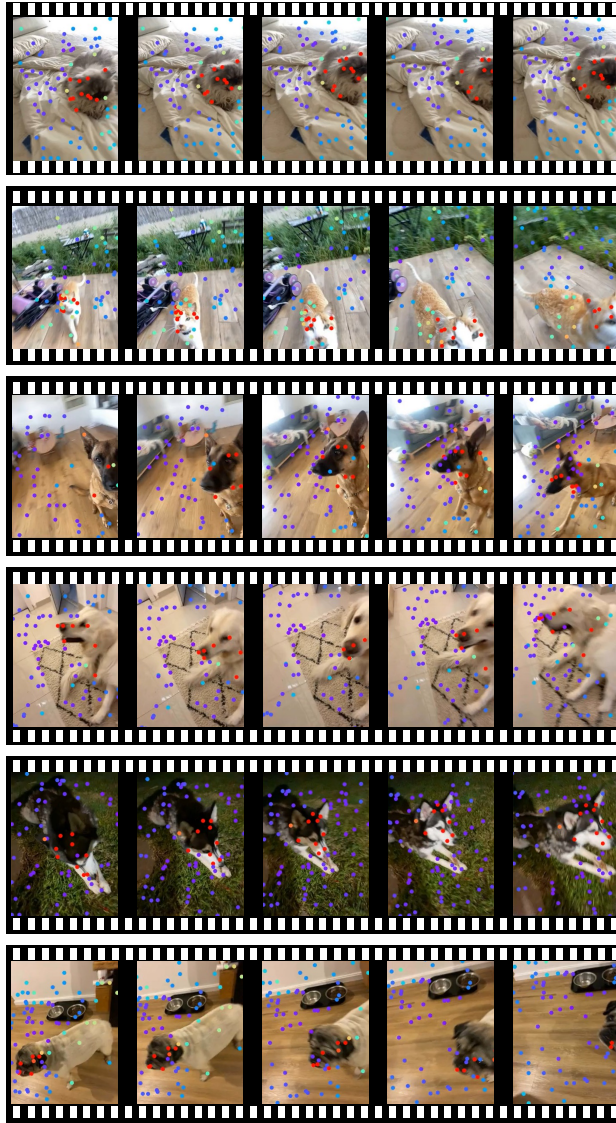


**Fig. 5:  $\gamma$  Visualization.** We show a visualization of the  $\gamma$  outputs of our network that are described in Sec. 4.2. In each video sequence, we show the input tracks, where each color visualizes its movement level value,  $\gamma$ . Purple marks rigid points with low  $\gamma$  whereas red marks non-rigid points with high  $\gamma$ . Note, that our network did not get any direct supervision for these values, but the raw point tracks predictions from [18]. To emphasize our generalization, the  $\gamma$  visualizations for cats were produced by the model that was only trained on dogs and vice versa.

## 5.4 Ablation Study

To evaluate the contribution of our different method parts we run an ablation study which is presented in Tab. 3. In this study, the training was always done on the cats partition from COP3D and evaluated on our test data which contains dogs and cats. More specifically, we ablate on our transformer architecture by taking the architecture suggested by [29] ("Set of Sets") or the DSS architecture [27] ("DSS"). As the table shows our architecture ("Full") achieved significantly better results. We further ignored the  $\gamma$  outputs and used regular reprojection error on  $B_1$  for all points ("No  $\gamma$ "). We further ablate our sparsity loss ("No  $\mathcal{L}_{\text{Sparse}}$ ") and the rigid loss ("No  $\mathcal{L}_{\text{Rigid}}$ "). In both cases, the error increased whereas in the later one, the results became much worse.

We further ablate the choice of  $K = 12$  as the number of non-rigid bases, by trying two extreme numbers of  $K = 30, K = 2$  (we saw no significant differences when we used nearby choices such as  $K = 11$ ). As can be seen in the table, when  $K = 30$  the output is not regularized enough and produces a higher depth error for the dynamic part. For  $K = 2$  the depth is regularized but the reprojection error ("Rep. (pix.)") gets higher due to over-regularization. Overall the ablation study justifies our design choices ("Full").

## 5.5 Limitations and Future Work

Our method cannot handle videos with too rapid motion, and in general, is limited by the accuracy of the tracking method [18]. We note that any future improvements with point tracking in terms of accuracy and inference time will directly improve our method as well.

Our method assumes enough motion parallax to constrain the depth values and fails to generate accurate camera poses without it. A future and interesting work would be to try combining depth-from-single-image prior as additional inputs to our network for handling cases with minimal motion parallax and for improving accuracies.

## 6 Conclusion

We presented TRACKSTO4D, a novel deep-learning framework that directly translates 2D motion tracks from casual videos into their corresponding non-rigid structure and motion. Our approach features a deep learning architecture that considers the symmetries in the problem with designed intrinsic constraints to handle the ill-posed nature of this problem. Notably, our network was trained using only raw supervision of 2D point tracks extracted by an off-the-shelf method [18] without any 3D supervision. Yet, it implicitly learned to predict camera poses and non-rigid structures while identifying the non-rigid parts. During inference, our method demonstrates faster processing times compared to previous methods while achieving comparable accuracy. Furthermore, our network exhibits strong generalization capabilities, performing well even on semantic categories that were not present in the training data.

*Acknowledgments* HM is the Robert J. Shillman Fellow, and is supported by the Israel Science Foundation through a personal grant (ISF 264/23) and an equipment grant (ISF 532/23).

## A Supplementary Results

### A.1 Video Results

We provide supplementary video outputs of several cases from our test set. Each video presents the input video frames with a set of pre-extracted point tracks that are used as input to our network and presented in corresponding colors (left side), and the output cameras and dynamic 3D structure (right side). The output camera trajectory is presented as gray frustums, whereas the current camera is marked in red. The reconstructed 3D scene points are presented in corresponding colors to the input tracks. Note that the outputs presented in the videos were obtained at inference time, with a single feed-forward prediction, without any optimization or fine-tuning, on unseen test cases.

### A.2 Extended Quantitative Evaluation

Per-sequence and mean quantitative comparisons for our 21 pet test videos are presented in Tab. 5 and Tab. 6. We also show per-sequence fine-tuned results of 2000 iterations starting from our final checkpoint. The fine-tuning is done as a post-processing by minimizing the original loss function on the given test video. This takes about 10 minutes per case which is still fast compared to the run time of the previous methods that predicted dynamic depths (see Tab. 1).

### A.3 Generalization Beyond Pet Videos

We further applied our pretrained network on the MPI Sintel dataset [9] for the evaluation set defined by [64] of 14 sequences. We note that the pet domain that was used for training our network is very different from the Sintel domain which contains fast motion of multiple characters. Yet, we can see that due to the strong prior collected by our network, it generalizes to some extent to the domain of Sintel. Fig. 6 shows a qualitative evaluation of our movement level predictions ( $\gamma$ ). As can be seen, despite the domain gap (compared to Fig. 5), our network identifies the non-rigid movement in the videos. We further evaluated the camera pose accuracy in Tab. 7. Even though our mean accuracy is not the best among all methods, our method gets the most accurate results on some metrics for several sequences. Training on a video dataset in a similar domain to Sintel could possibly improve the generalization of our method for Sintel. Unfortunately, the Sintel dataset contains only 23 sequences.

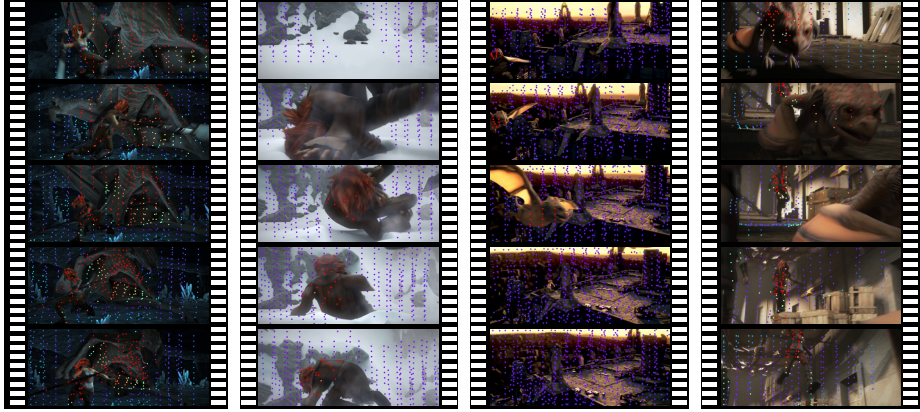


**Fig. 6:  $\gamma$  Visualization for Sintel.** We show a visualization of the  $\gamma$  outputs of our network. In each video sequence, we show the input tracks, where each color visualizes its movement level value,  $\gamma$ . Purple marks rigid points with low  $\gamma$  whereas red marks non-rigid points with high  $\gamma$ . Note that our network was only trained on pet videos, and did not see any videos in the domain of Sintel. Yet, at inference time with no further optimization, it identifies the non-rigid movement successfully.

## B Implementation Details

### B.1 Architecture

Here we provide a precise definition for our equivariant layer:  $F : \mathbb{R}^{N \times P \times d} \rightarrow \mathbb{R}^{N \times P \times d}$ . The computation of  $F$  is split into four steps, as described below:

$$\bar{\mathbf{q}}_{ij} = \bar{W}^Q M_{ij}, \bar{\mathbf{k}}_{ij} = \bar{W}^K M_{ij}, \bar{\mathbf{v}}_{ij} = \bar{W}^V M_{ij}, \quad (12a)$$

$$\bar{M}_{ij} = \sum_{i'=1}^N \frac{\exp(\bar{\mathbf{q}}_{ij} \cdot \bar{\mathbf{k}}_{i'j})}{\sum_{l=1}^N \exp(\bar{\mathbf{q}}_{ij} \cdot \bar{\mathbf{k}}_{lj})} \bar{\mathbf{v}}_{i'j} \quad (12b)$$

$$\mathbf{q}_{ij} = W^Q \bar{M}_{ij}, \mathbf{k}_{ij} = W^K \bar{M}_{ij}, \mathbf{v}_{ij} = W^V \bar{M}_{ij}, \quad (12c)$$

$$F(M)_{ij} = \sum_{j'=1}^P \frac{\exp(\mathbf{q}_{ij} \cdot \mathbf{k}_{ij'})}{\sum_{l=1}^P \exp(\mathbf{q}_{ij} \cdot \mathbf{k}_{il})} \mathbf{v}_{ij'} \quad (12d)$$

Here,  $M_{i,j} \in \mathbb{R}^d$  are the features associated with the  $j$ -th point in the  $i$ -th frame. The attention mechanism defined in the first two equations above (with additional temporal positional encoding) replaces the translation equivariant function  $L$  applied to the columns of  $M$  (Eq.(3)), and the attention in the last two equations above implements the point cloud aggregation (summation) (also in Eq.(3)) applied to the rows of  $M$ . As commonly done we use 16 attention head transformations [46]. We add standard temporal positional encoding for



	Grid size	ATE ↓ (mm)	RPE Trans ↓ (mm)	RPE Rot ↓ (deg)	Inference ↓ Time
Ours (cats only)	15	8.96	3.79	0.23	0.16(+8.6) seconds
Ours (cats only)+BA	15	4.22	2.86	0.17	0.40(+8.6) seconds
Ours (cats only)	12	9.18	3.81	0.24	0.09(+7.8) seconds
Ours (cats only)+BA	12	4.36	2.97	0.17	0.24(+7.8) seconds
Ours (cats only)	10	8.91	3.91	0.23	0.05(+7.7) seconds
Ours (cats only)+BA	10	4.44	3.01	0.18	0.16(+7.7) seconds
Ours (cats only)	7	9.06	4.11	0.25	0.02(+7.6) seconds
Ours (cats only)+BA	7	4.93	3.52	0.20	0.08(+7.6) seconds
Ours (cats only)	5	10.29	4.97	0.31	0.01(+7.6) seconds
Ours (cats only)+BA	5	8.08	6.33	0.38	0.05(+7.6) seconds

**Table 4: Tracking Grid Size Effect** Quantitative evaluation of the effect of reducing the number of sampled point tracks at inference time. We measure the camera pose accuracy and the running time. We also mention the point tracks extraction time in parenthesis (e.g. +8.6 seconds) which is performed by [18] as a preprocess. As can be seen, our method can handle a smaller number of points but the accuracy slightly drops with fewer sampled points

the transformers with respect to the  $N$  (time) dimension as described in [46]. In our implementation, we added positional encoding only in the first layer.

*Architecture Technical Details* For learning high frequencies we map each input coordinate to sinusoidal functions as in [28] with  $L = 12$ . We use 3 pairs of attention layers, each of frames attention followed by point attention. Each point (after sinusoidal functions embedding) is mapped into  $\mathbb{R}^{256}$  with a linear layer. Each attention layer is a function of the form  $F : \mathbb{R}^{N \times P \times 256} \rightarrow \mathbb{R}^{N \times P \times 256}$  (see details above). Each attention uses 16 heads with  $K, Q, V \in \mathbb{R}^{(N \text{ or } P) \times 64}$  followed by a fully connected network with 1 hidden layer of 2048 features. We then average over the rows to get per-point features  $P_0 \in \mathbb{R}^{P \times 256}$  and over the columns to get per-frame features  $F_0 \in \mathbb{R}^{N \times 256}$ . Finally, we map  $P_0$  to per-point outputs  $P_1 \in \mathbb{R}^{P \times (3K+1)}$  ( $K$  basis points and  $\gamma$ ) with a linear layer, and  $F_0$  into per-camera outputs  $F_1 \in \mathbb{R}^{N \times (6+3+K)}$  (6 for the rotation parameters [67], 3 for the camera center, and  $K$  coefficients) using a conv layer with a kernel size of 31.

## B.2 Other Implementation Details

*Point Tracks Sampling* For building  $M \in \mathbb{R}^{N \times P \times 3}$  we use the implementation of [18]. We sample a uniform grid of  $15 \times 15$  2D points, starting from frame number 0, 20, 40, ..., and then track these points throughout the entire video (backward and forward). In Tab. 4 we show the effect of reducing the grid size at inference time, in terms of camera pose accuracy and running time. During training, at each iteration, we randomly sample 20-50 frames from the training

videos and 100 point tracks, i.e.  $20 \leq N \leq 50$  and  $P = 100$ . When sampling cameras and point tracks of size  $N \times P$  from a larger matrix of size  $N' \times P'$  we only take a point track if its starting tracking time is in the range  $[t - \frac{N}{2}, t + \frac{3N}{2}]$ , where  $t$  is the first sampled index. At inference time we take all the available point tracks. In both, training and inference time, we keep only point tracks that are observed in more than 10 frames.

*Test Set* We used the RGBD camera of the iPhone 11 to record our 21 test videos of dogs and cats. Each frame has a resolution of  $640 \times 480$  pixels. Note that the training set contained various types of resolutions. All pet owners who were photographed gave their permission for the animals to be photographed. For evaluation only, we define a point track as dynamic if its associated GT mask value is 1 for at least 40 frames. The GT masks are obtained by running [68] and searching for labels of dogs and cats. They were only used for evaluation and not used by our method at all.

*Bundle Adjustment* After inference, as optional refinement, we take the output rigid approximation  $B_1 \in \mathbb{R}^{P \times 3}$  and the output camera poses  $\{R_1, \dots, R_N\}$ ,  $\{\mathbf{t}_1, \dots, \mathbf{t}_N\}$  and apply Bundle Adjustment (BA). We use a 3D world point from  $B_1$  if its associated  $\gamma$  is below 0.008. We optimize reprojection errors of a given observation  $M_{i,j}$ , only if it is observed, i.e.  $M_{i,j}^o = 1$  and if the initial reprojection error is below 10 pixels. We use the BA implementation provided by [29], which is based on the Ceres package [2].

*Training Technical Details* In all training setups, we used:  $\lambda_{\text{Reprojection}} = 50.0$ ,  $\lambda_{\text{Rigid}} = 1.0$ ,  $\lambda_{\text{Negative}} = 1.0$ ,  $\lambda_{\text{Sparse}} = 0.001$ . At the beginning of the training, we pre-train the camera poses to be located behind and facing the origin. This prevents cases in which the cameras are located in the middle of the initial point cloud s.t. many points have negative depths, which may result in bad convergence. More specifically, the pre-train loss is:

$$\mathcal{L}_{\text{Pretrain}} = \frac{1}{N} \sum_{i=1}^N \frac{1}{100} \|\mathbf{t}_i - [0, 0, -15]^T\|^2 + \|R_i - I\|_F^2$$

The pretrain runs until convergence ( $\mathcal{L}_{\text{Pretrain}} < 10^{-4}$ ). During the main training, we detach gradients from  $B_1$  and  $(R_1, \mathbf{t}_1) \dots, (R_N, \mathbf{t}_N)$  for  $\mathcal{L}_{\text{Reproject}}$  to stabilize the training. Until epoch 50 we sample sequences of  $N$  in the range [20, 22], and then we increase the range to [20, 50].



		All	<b>1.00</b>	0.95	<b>1.00</b>	<b>1.00</b>	<b>1.00</b>	<b>1.00</b>	<b>1.00</b>	<b>1.00</b>
Seq11	Abs Rel↓	Dyn	0.34	0.14	<b>0.06</b>	0.10	0.07	0.10	0.07	0.10
		All	0.17	0.38	<b>0.05</b>	0.08	<b>0.05</b>	0.07	<b>0.05</b>	<b>0.05</b>
	$\delta < 1.25 \uparrow$	Dyn	0.47	0.79	<b>0.92</b>	0.90	<b>0.92</b>	0.90	<b>0.92</b>	0.90
		All	0.74	0.67	<b>0.97</b>	0.90	0.96	0.94	0.96	0.96
	$\delta < 1.25^2 \uparrow$	Dyn	0.86	<b>1.00</b>		0.99	0.96	0.98	0.97	0.98
		All	0.94	0.78	0.99	0.99	<b>1.00</b>	0.99	0.99	0.99
Seq12	$\delta < 1.25^3 \uparrow$	Dyn	0.94	<b>1.00</b>		0.99	0.99	<b>1.00</b>	0.99	<b>1.00</b>
		All	0.99	0.86	<b>1.00</b>	<b>1.00</b>	<b>1.00</b>	<b>1.00</b>	<b>1.00</b>	<b>1.00</b>
	Abs Rel↓	Dyn	0.37	0.16	0.05	0.10	0.05	0.09	0.04	0.04
		All	0.16	0.13	<b>0.05</b>	<b>0.08</b>	0.08	0.08	0.08	0.08
	$\delta < 1.25 \uparrow$	Dyn	0.19	0.79	<b>0.98</b>	<b>0.98</b>	0.97	<b>0.98</b>	0.97	0.97
		All	0.73	0.85	<b>0.98</b>	0.95	0.94	0.95	0.94	0.94
Seq13	$\delta < 1.25^2 \uparrow$	Dyn	0.97	<b>1.00</b>		<b>1.00</b>	<b>1.00</b>	<b>1.00</b>	<b>1.00</b>	<b>1.00</b>
		All	0.98	0.98	<b>1.00</b>	0.99	0.97	0.99	0.99	0.97
	$\delta < 1.25^3 \uparrow$	Dyn	<b>1.00</b>	<b>1.00</b>		<b>1.00</b>	<b>1.00</b>	<b>1.00</b>	<b>1.00</b>	<b>1.00</b>
		All	<b>1.00</b>	<b>1.00</b>	<b>1.00</b>	<b>1.00</b>	0.98	<b>1.00</b>	<b>1.00</b>	0.98
	Abs Rel↓	Dyn	0.31	0.29	<b>0.09</b>	0.15	0.11	0.14	0.10	0.10
		All	3.31E+08	0.35	<b>0.06</b>	0.10	0.08	0.09	0.07	0.07
Seq14	$\delta < 1.25 \uparrow$	Dyn	0.50	0.50	0.93	0.82	0.95	0.85	<b>0.96</b>	<b>0.96</b>
		All	0.67	0.69	<b>0.97</b>	0.91	<b>0.97</b>	0.93	<b>0.97</b>	<b>0.97</b>
	$\delta < 1.25^2 \uparrow$	Dyn	0.81	0.84	<b>1.00</b>	<b>1.00</b>	<b>1.00</b>	<b>1.00</b>	<b>1.00</b>	<b>1.00</b>
		All	0.81	0.87	<b>0.99</b>	0.98	<b>0.99</b>	<b>0.99</b>	<b>0.99</b>	<b>0.99</b>
	$\delta < 1.25^3 \uparrow$	Dyn	<b>1.00</b>	<b>1.00</b>		<b>1.00</b>	<b>1.00</b>	<b>1.00</b>	<b>1.00</b>	<b>1.00</b>
		All	0.87	0.93	<b>1.00</b>	0.99	0.99	0.99	0.99	0.99
Seq15	Abs Rel↓	Dyn	0.18	0.17	<b>0.03</b>	0.05	<b>0.03</b>	0.04	0.04	0.04
		All	0.18	0.34	<b>0.03</b>	0.04	<b>0.03</b>	<b>0.03</b>	<b>0.03</b>	<b>0.03</b>
	$\delta < 1.25 \uparrow$	Dyn	0.79	0.72	<b>0.99</b>	<b>0.99</b>	<b>0.99</b>	<b>0.99</b>	<b>0.99</b>	<b>0.99</b>
		All	0.76	0.55	<b>1.00</b>	0.99	0.99	0.99	0.99	0.99
	$\delta < 1.25^2 \uparrow$	Dyn	0.93	0.97	<b>1.00</b>	<b>1.00</b>	<b>1.00</b>	<b>1.00</b>	<b>1.00</b>	<b>1.00</b>
		All	0.94	0.83	<b>1.00</b>	<b>1.00</b>	<b>1.00</b>	<b>1.00</b>	<b>1.00</b>	<b>1.00</b>
Seq16	$\delta < 1.25^3 \uparrow$	Dyn	0.99	<b>1.00</b>		<b>1.00</b>	<b>1.00</b>	<b>1.00</b>	<b>1.00</b>	<b>1.00</b>
		All	0.99	0.92	<b>1.00</b>	<b>1.00</b>	<b>1.00</b>	<b>1.00</b>	<b>1.00</b>	<b>1.00</b>
	Abs Rel↓	Dyn	1.22	<b>0.12</b>	0.15	0.27	0.13	0.18	0.13	0.13
		All	0.33	0.39	<b>0.09</b>	0.15	0.11	0.18	0.10	0.10
	$\delta < 1.25 \uparrow$	Dyn	0.01	0.77	<b>0.95</b>	0.62	0.90	0.79	0.88	0.88
		All	0.65	0.65	<b>0.97</b>	0.80	0.93	0.70	0.93	0.93
Seq17	$\delta < 1.25^2 \uparrow$	Dyn	0.12	<b>1.00</b>	0.99	0.93	0.99	0.96	0.99	0.99
		All	0.81	0.83	<b>0.99</b>	0.97	0.98	0.92	0.98	0.98
	$\delta < 1.25^3 \uparrow$	Dyn	0.46	<b>1.00</b>	0.99	<b>1.00</b>	0.99	<b>1.00</b>	0.99	0.99
		All	0.90	0.89	<b>0.99</b>	<b>0.99</b>	0.98	<b>0.99</b>	<b>0.99</b>	<b>0.99</b>
	Abs Rel↓	Dyn	0.28	0.12	<b>0.07</b>	0.14	0.12	0.14	0.12	0.12
		All	0.21	0.21	<b>0.05</b>	0.06	0.06	0.06	0.06	0.06
Seq18	$\delta < 1.25 \uparrow$	Dyn	0.42	0.92	<b>0.98</b>	0.81	0.89	0.80	0.90	0.90
		All	0.66	0.79	<b>0.99</b>	0.96	0.97	0.96	0.97	0.97
	$\delta < 1.25^2 \uparrow$	Dyn	0.98	<b>1.00</b>	<b>1.00</b>	<b>1.00</b>	<b>1.00</b>	<b>1.00</b>	<b>1.00</b>	<b>1.00</b>
		All	0.95	0.93	<b>1.00</b>	<b>1.00</b>	<b>1.00</b>	<b>1.00</b>	<b>1.00</b>	<b>1.00</b>
	$\delta < 1.25^3 \uparrow$	Dyn	<b>1.00</b>	<b>1.00</b>		<b>1.00</b>	<b>1.00</b>	<b>1.00</b>	<b>1.00</b>	<b>1.00</b>
		All	<b>1.00</b>	0.96	<b>1.00</b>	<b>1.00</b>	<b>1.00</b>	<b>1.00</b>	<b>1.00</b>	<b>1.00</b>
Seq19	Abs Rel↓	Dyn	0.35	0.12	0.14	<b>0.11</b>	0.12	0.11	0.12	0.12
		All	0.23	0.15	0.08	0.07	0.07	0.07	<b>0.06</b>	<b>0.06</b>
	$\delta < 1.25 \uparrow$	Dyn	0.40	0.88	0.76	<b>0.93</b>	0.87	0.91	0.88	0.88
		All	0.60	0.81	0.89	<b>0.94</b>	<b>0.94</b>	0.93	<b>0.94</b>	<b>0.94</b>
	$\delta < 1.25^2 \uparrow$	Dyn	0.82	<b>0.99</b>	0.98	<b>0.99</b>	0.98	0.98	0.98	0.98
		All	0.87	0.94	0.98	0.98	<b>0.99</b>	<b>0.99</b>	<b>0.99</b>	<b>0.99</b>
Seq20	$\delta < 1.25^3 \uparrow$	Dyn	0.95	<b>1.00</b>	<b>1.00</b>	0.99	<b>1.00</b>	0.99	<b>1.00</b>	<b>1.00</b>
		All	0.95	0.98	<b>1.00</b>	0.99	<b>1.00</b>	<b>1.00</b>	<b>1.00</b>	<b>1.00</b>
	Abs Rel↓	Dyn	0.48	0.21	0.10	0.12	<b>0.07</b>	0.11	0.08	0.08
		All	0.14	0.32	<b>0.05</b>	0.10	0.09	0.08	0.09	0.09
	$\delta < 1.25 \uparrow$	Dyn	0.46	0.60	0.93	0.87	<b>0.95</b>	0.88	<b>0.95</b>	<b>0.95</b>
		All	0.86	0.65	<b>0.98</b>	0.91	0.96	0.95	0.96	0.96
Seq21	$\delta < 1.25^2 \uparrow$	Dyn	0.55	0.95	0.98	<b>1.00</b>	0.99	0.99	0.99	0.99
		All	0.91	0.84	<b>0.99</b>	0.98	0.98	0.98	0.98	0.98
	$\delta < 1.25^3 \uparrow$	Dyn	0.84	<b>1.00</b>	0.99	<b>1.00</b>	<b>1.00</b>	<b>1.00</b>	<b>1.00</b>	<b>1.00</b>
		All	0.97	0.92	<b>1.00</b>	0.99	0.98	0.99	0.98	0.98
	Abs Rel↓	Dyn	0.33	0.14	0.06	<b>0.04</b>	0.05	0.05	0.05	0.05
		All	0.15	0.27	<b>0.03</b>	<b>0.03</b>	<b>0.03</b>	0.05	<b>0.03</b>	<b>0.03</b>
Seq22	$\delta < 1.25 \uparrow$	Dyn	0.28	0.80	0.97	0.97	0.97	<b>0.98</b>	0.97	0.97
		All	0.81	0.74	<b>0.99</b>	<b>0.99</b>	<b>0.99</b>	<b>0.99</b>	<b>0.99</b>	<b>0.99</b>
	$\delta < 1.25^2 \uparrow$	Dyn	0.91	0.97	<b>1.00</b>	<b>1.00</b>	0.99	0.99	0.99	0.99
		All	0.98	0.87	<b>1.00</b>	<b>1.00</b>	<b>1.00</b>	<b>1.00</b>	<b>1.00</b>	<b>1.00</b>
	$\delta < 1.25^3 \uparrow$	Dyn	<b>1.00</b>	0.99	<b>1.00</b>	<b>1.00</b>	<b>1.00</b>	<b>1.00</b>	<b>1.00</b>	<b>1.00</b>
		All	<b>1.00</b>	0.92	<b>1.00</b>	<b>1.00</b>	<b>1.00</b>	<b>1.00</b>	<b>1.00</b>	<b>1.00</b>
Seq23	Abs Rel↓	Dyn	0.33	0.27	<b>0.21</b>	0.27	0.28	0.26	0.29	0.29
		All	2.42E+08	0.45	<b>0.04</b>	0.05	0.05	0.05	0.05	0.05
	$\delta < 1.25 \uparrow$	Dyn	0.34	0.49	<b>0.61</b>	0.44	0.38	0.49	0.34	0.34
		All	0.50	0.42	<b>0.97</b>	0.95	0.95	0.95	0.95	0.95
	$\delta < 1.25^2 \uparrow$	Dyn	0.93	0.90	<b>1.00</b>	<b>1.00</b>	<b>1.00</b>	<b>1.00</b>	<b>1.00</b>	<b>1.00</b>
		All	0.77	0.72	<b>1.00</b>	<b>1.00</b>	<b>1.00</b>	<b>1.00</b>	<b>1.00</b>	<b>1.00</b>
Mean	$\delta < 1.25^3 \uparrow$	Dyn	0.99	0.99	<b>1.00</b>	<b>1.00</b>	<b>1.00</b>	<b>1.00</b>	<b>1.00</b>	<b>1.00</b>
		All	0.83	0.85	<b>1.00</b>	<b>1.00</b>	<b>1.00</b>	<b>1.00</b>	<b>1.00</b>	<b>1.00</b>
	Abs Rel↓	Dyn	0.40	0.16	<b>0.09</b>	0.12	<b>0.09</b>	0.11	<b>0.09</b>	<b>0.09</b>
		All	3.63E+07	6.16E+04	<b>0.06</b>	0.08	<b>0.06</b>	0.08	<b>0.06</b>	<b>0.06</b>
	$\delta < 1.25 \uparrow$	Dyn	0.43	0.78	<b>0.93</b>	0.85	0.90	0.88	0.89	0.89
		All	0.72	0.71	<b>0.97</b>	0.91	0.96	0.92	0.96	0.96
Mean	$\delta < 1.25^2 \uparrow$	Dyn	0.75	0.97	0.99	0.98	<b>1.00</b>	0.99	<b>1.00</b>	<b>1.00</b>
		All	0.90	0.88	<b>0.99</b>	0.98	<b>0.99</b>	0.98	<b>0.99</b>	<b>0.99</b>
	$\delta < 1.25^3 \uparrow$	Dyn	0.92	<b>1.00</b>	<b>1.00</b>	<b>1.00</b>	<b>1.00</b>	<b>1.00</b>	<b>1.00</b>	<b>1.00</b>
		All	0.96	0.93	<b>1.00</b>	<b>1.00</b>	0.99	<b>1.00</b>	0.99	0.99

**Table 5: Depth Accuracy.** We show a comparison to previous methods on the predicted depth for the point trajectories compared to their GT depths. We compare 4 ways of running our method. Ours (C&D), Ours (C): Our inference time outputs for a model that was trained on cats and dogs or only on cats respectively. Ours (C&D) FT, Ours (C) FT: The outputs of our model trained on cats and dogs or cats respectively, after fine-tuning our losses for each specific video. As can be seen, fine-tuning improves our accuracy even more.

		DROID-SLAM [43]	ParticleSfM [64]	RCVD [21]	CasualSAM [62]	Ours (C)	Ours (C)+BA	Ours (Csho)+FT
Seq0	ATE(mm)	<b>3.71</b>	6.10	64.67	5.36	5.60	5.43	4.40
	RPE T.(mm)	3.05	3.22	26.92	3.13	3.63	3.04	<b>2.91</b>
	RPE R.(deg.)	0.14	0.18	2.53	0.16	0.22	0.15	<b>0.13</b>
Seq1	ATE(mm)	1.91	3.83	38.44	10.28	13.21	4.32	<b>1.71</b>
	RPE T.(mm)	1.32	1.49	25.23	3.00	2.65	1.72	<b>1.29</b>
	RPE R.(deg.)	0.18	0.23	2.43	0.67	0.29	0.19	<b>0.16</b>
Seq2	ATE(mm)	3.13	4.68	39.46	<b>2.13</b>	4.57	2.78	2.52
	RPE T.(mm)	3.62	5.82	27.27	<b>1.97</b>	3.24	2.62	2.55
	RPE R.(deg.)	0.08	0.21	1.89	<b>0.06</b>	0.12	0.09	0.09
Seq3	ATE(mm)	5.13	<b>2.26</b>	29.55	2.49	7.83	2.66	2.87
	RPE T.(mm)	5.76	<b>2.00</b>	24.18	2.51	3.13	2.27	2.38
	RPE R.(deg.)	0.17	<b>0.07</b>	2.38	0.08	0.13	<b>0.07</b>	<b>0.07</b>
Seq4	ATE(mm)	2.59	4.38	56.16	2.65	4.21	2.38	<b>2.24</b>
	RPE T.(mm)	2.05	2.07	21.36	<b>1.74</b>	2.40	2.05	1.95
	RPE R.(deg.)	0.11	0.11	1.05	<b>0.09</b>	0.15	0.11	0.10
Seq5	ATE(mm)	1.07	0.83	14.22	<b>0.53</b>	1.44	0.79	0.74
	RPE T.(mm)	1.02	0.74	6.51	<b>0.52</b>	0.88	0.68	0.68
	RPE R.(deg.)	0.09	0.07	1.63	<b>0.05</b>	0.12	0.07	0.06
Seq6	ATE(mm)	<b>26.08</b>	31.07	48.31	26.12	27.10	28.28	29.80
	RPE T.(mm)	10.57	11.01	24.21	<b>10.31</b>	10.44	10.92	11.02
	RPE R.(deg.)	0.66	0.67	4.03	<b>0.62</b>	0.69	0.69	0.68
Seq7	ATE(mm)	2.25	28.48	47.25	<b>1.78</b>	4.53	2.39	2.11
	RPE T.(mm)	2.34	6.13	23.81	<b>1.72</b>	2.32	1.98	1.95
	RPE R.(deg.)	0.15	0.59	2.29	<b>0.11</b>	0.20	0.16	0.15
Seq8	ATE(mm)	1.23	38.79	44.06	2.00	4.78	<b>0.84</b>	0.96
	RPE T.(mm)	1.07	50.57	25.46	1.24	1.54	<b>0.71</b>	0.74
	RPE R.(deg.)	0.07	4.78	1.73	0.09	0.13	0.06	<b>0.05</b>
Seq9	ATE(mm)	21.74	18.52	43.45	34.93	24.15	3.92	<b>3.28</b>
	RPE T.(mm)	9.04	7.96	21.35	21.06	6.89	2.77	<b>2.01</b>
	RPE R.(deg.)	0.62	0.47	3.47	0.71	0.37	0.12	<b>0.10</b>
Seq10	ATE(mm)	1.47	1.75	22.49	<b>1.40</b>	3.03	1.42	1.48
	RPE T.(mm)	1.84	1.15	24.22	<b>1.11</b>	1.87	1.25	1.24
	RPE R.(deg.)	0.22	0.12	2.18	<b>0.10</b>	0.21	0.12	0.12
Seq11	ATE(mm)	1.71	3.60	19.10	<b>1.32</b>	3.12	1.66	1.50
	RPE T.(mm)	1.65	1.54	16.34	<b>1.21</b>	3.12	1.75	1.60
	RPE R.(deg.)	0.08	0.08	1.80	<b>0.06</b>	0.12	0.08	0.07
Seq12	ATE(mm)	<b>1.70</b>	3.64	20.82	2.51	6.23	3.61	2.58
	RPE T.(mm)	<b>2.24</b>	2.63	18.50	2.74	4.04	3.02	2.34
	RPE R.(deg.)	<b>0.09</b>	0.12	2.03	0.12	0.23	0.15	0.14
Seq13	ATE(mm)	1.23	2.38	33.49	1.49	4.10	<b>1.17</b>	1.27
	RPE T.(mm)	1.19	1.40	17.33	<b>1.00</b>	1.72	1.12	1.01
	RPE R.(deg.)	0.13	0.14	2.12	0.12	0.19	0.12	<b>0.11</b>
Seq14	ATE(mm)	5.42	5.15	1.05E+02	24.95	6.09	5.06	<b>4.90</b>
	RPE T.(mm)	3.40	<b>3.38</b>	69.36	9.45	4.07	3.57	3.55
	RPE R.(deg.)	<b>0.18</b>	0.19	3.81	0.65	0.26	0.20	0.19
Seq15	ATE(mm)	7.69	61.06	36.70	7.40	36.51	<b>4.98</b>	5.50
	RPE T.(mm)	7.95	17.57	28.18	6.93	10.19	5.86	<b>5.74</b>
	RPE R.(deg.)	0.22	0.58	2.85	0.19	0.30	0.16	<b>0.15</b>
Seq16	ATE(mm)	5.04	5.06	36.42	<b>3.69</b>	4.52	4.11	3.81
	RPE T.(mm)	4.53	4.54	20.11	<b>4.02</b>	4.47	4.25	4.25
	RPE R.(deg.)	0.28	0.29	2.94	<b>0.25</b>	0.31	0.28	0.28
Seq17	ATE(mm)	<b>1.12</b>	34.07	77.91	1.49	6.52	2.51	2.89
	RPE T.(mm)	<b>1.15</b>	12.30	39.64	1.18	2.14	1.50	1.47
	RPE R.(deg.)	0.10	1.11	2.20	<b>0.08</b>	0.17	0.13	0.13
Seq18	ATE(mm)	<b>2.98</b>	6.25	36.54	4.91	7.73	4.13	3.83
	RPE T.(mm)	4.05	5.21	24.78	3.89	4.34	<b>3.62</b>	3.80
	RPE R.(deg.)	0.23	0.29	1.67	<b>0.21</b>	0.24	<b>0.21</b>	<b>0.21</b>
Seq19	ATE(mm)	<b>1.45</b>	2.23	42.95	1.82	8.51	2.79	2.39
	RPE T.(mm)	1.65	1.72	29.12	<b>1.44</b>	3.23	2.21	1.97
	RPE R.(deg.)	0.11	0.11	2.09	<b>0.09</b>	0.25	0.16	0.14
Seq20	ATE(mm)	8.13	4.37	66.03	4.95	4.30	<b>3.43</b>	4.03
	RPE T.(mm)	6.20	3.57	27.34	<b>3.00</b>	3.30	3.05	3.08
	RPE R.(deg.)	0.36	0.20	1.35	<b>0.18</b>	0.20	<b>0.18</b>	<b>0.18</b>
Mean	ATE(mm)	5.08	12.79	43.95	6.90	8.96	4.22	<b>4.04</b>
	RPE T.(mm)	3.60	6.95	25.77	3.95	3.79	2.86	<b>2.74</b>
	RPE R.(deg.)	0.20	0.51	2.31	0.22	0.23	0.17	<b>0.16</b>

**Table 6: Camera Poses Accuracy.** We show a comparison to previous methods on the predicted camera poses. We compare 3 ways of running our method. Ours (C): Our inference time outputs (total inference time of 0.16 seconds) for a model that was trained only on cats. Ours (C)+BA: Our inference time outputs, followed by a short Bundle Adjustment (total inference time of 0.4 seconds) for a model that was trained only on cats. Ours (C) FT: The outputs of the model that was trained only on cats after fine-tuning our losses for each specific video (total running time of about 10 minutes). As can be seen, after BA, our results are the most accurate compared to the other methods, and fine-tuning improves our accuracy even more.

		RCVD [21]	DROID-SLAM [43]	Particle SfM [64]	CasualSAM [62]	Ours (C)	Ours (C)+BA	Ours (C&D)	Ours (C&D)+BA
alley_2	ATE(mm)	0.026	0.057	0.002	<b>0.0008</b>	0.043	0.027	0.055	0.046
	RPE T. (mm)	0.056	0.035	0.0007	<b>0.0004</b>	0.033	0.040	0.034	0.041
	RPE R. (deg.)	0.821	1.047	0.009	<b>0.008</b>	0.468	0.507	0.511	0.531
ambush_4	ATE(mm)	0.171	0.104	0.068	<b>0.011</b>	0.050	0.021	0.055	0.022
	RPE T. (mm)	0.048	0.035	0.027	<b>0.007</b>	0.026	0.026	0.026	0.026
	RPE R. (deg.)	3.025	1.385	0.473	<b>0.079</b>	0.398	0.319	0.382	0.324
ambush_5	ATE(mm)	0.230	0.112	<b>0.002</b>	0.008	0.057	0.010	0.035	0.009
	RPE T. (mm)	0.046	0.029	<b>0.001</b>	0.003	0.018	0.008	0.015	0.006
	RPE R. (deg.)	4.105	1.580	<b>0.055</b>	0.084	0.430	0.228	0.338	0.149
ambush_6	ATE(mm)	0.199	0.289	0.269	<b>0.042</b>	0.241	0.225	0.191	0.141
	RPE T. (mm)	0.112	0.078	0.081	<b>0.024</b>	0.088	0.129	0.072	0.078
	RPE R. (deg.)	4.147	4.596	0.951	<b>0.482</b>	1.928	3.364	1.602	1.849
cave_2	ATE(mm)	0.596	0.351	0.961	0.967	<b>0.217</b>	<b>0.217</b>	0.460	0.460
	RPE T. (mm)	0.171	0.172	0.142	0.170	<b>0.094</b>	<b>0.094</b>	0.113	0.113
	RPE R. (deg.)	7.508	5.489	3.678	2.674	<b>1.781</b>	<b>1.781</b>	2.634	2.634
cave_4	ATE(mm)	0.179	0.155	0.068	0.099	0.055	<b>0.008</b>	0.115	0.025
	RPE T. (mm)	0.087	0.035	0.012	<b>0.003</b>	0.024	0.006	0.028	0.021
	RPE R. (deg.)	2.040	2.710	0.409	0.052	0.244	<b>0.044</b>	0.294	0.171
market_2	ATE(mm)	0.032	0.011	0.003	<b>0.001</b>	0.027	0.002	0.033	0.003
	RPE T. (mm)	0.018	0.006	0.010	<b>0.0006</b>	0.004	0.002	0.007	0.002
	RPE R. (deg.)	0.141	0.035	0.041	0.010	0.107	<b>0.008</b>	0.091	<b>0.008</b>
market_5	ATE(mm)	1.213	0.912	0.012	<b>0.005</b>	0.891	1.187	0.859	0.525
	RPE T. (mm)	0.762	0.293	0.006	<b>0.002</b>	0.212	0.557	0.209	0.395
	RPE R. (deg.)	1.863	3.334	0.034	<b>0.015</b>	1.252	6.946	1.489	3.285
market_6	ATE(mm)	0.248	0.057	0.018	<b>0.008</b>	0.187	0.163	0.220	0.152
	RPE T. (mm)	0.214	0.037	0.007	<b>0.002</b>	0.103	0.097	0.095	0.086
	RPE R. (deg.)	0.817	1.296	0.120	<b>0.019</b>	1.003	0.850	0.834	0.695
shaman_3	ATE(mm)	0.054	0.001	<b>0.0005</b>	0.002	0.002	0.002	0.003	0.002
	RPE T. (mm)	0.023	0.002	<b>0.0004</b>	<b>0.0004</b>	0.0007	<b>0.0004</b>	0.001	<b>0.0004</b>
	RPE R. (deg.)	0.718	0.199	0.072	<b>0.036</b>	0.060	0.042	0.087	0.039
sleeping_1	ATE(mm)	0.029	0.011	0.008	0.008	<b>0.002</b>	<b>0.002</b>	<b>0.002</b>	<b>0.002</b>
	RPE T. (mm)	0.019	0.006	0.001	0.001	0.001	<b>0.0006</b>	0.001	<b>0.0006</b>
	RPE R. (deg.)	0.668	0.479	0.042	<b>0.040</b>	0.070	<b>0.040</b>	0.096	<b>0.040</b>
sleeping_2	ATE(mm)	0.043	0.005	0.0007	<b>0.0002</b>	0.005	0.006	0.005	0.006
	RPE T. (mm)	0.049	0.018	<b>0.0002</b>	<b>0.0002</b>	0.003	0.0007	0.003	0.0007
	RPE R. (deg.)	0.446	0.139	<b>0.006</b>	0.008	0.108	0.018	0.088	0.018
temple_2	ATE(mm)	1.245	0.073	0.011	0.086	0.189	0.011	0.217	<b>0.009</b>
	RPE T. (mm)	0.394	0.348	<b>0.002</b>	0.008	0.029	0.004	0.032	0.003
	RPE R. (deg.)	1.318	1.298	0.019	0.131	0.287	0.019	0.340	<b>0.018</b>
temple_3	ATE(mm)	0.769	<b>0.310</b>	0.381	0.587	0.350	0.510	0.329	0.473
	RPE T. (mm)	0.161	<b>0.093</b>	0.149	0.136	0.114	0.190	0.114	0.138
	RPE R. (deg.)	20.592	3.230	1.583	<b>0.109</b>	1.672	2.110	1.458	1.176
Mean	ATE(mm)	0.360	0.175	0.129	<b>0.124</b>	0.165	0.170	0.184	0.133
	RPE T. (mm)	0.154	0.085	0.031	<b>0.025</b>	0.054	0.082	0.054	0.065
	RPE R. (deg.)	3.444	1.916	0.535	<b>0.268</b>	0.701	1.163	0.732	0.781

**Table 7: Camera Poses Accuracy on Sintel.** We show a comparison to previous methods on the predicted camera poses. We compare 4 ways of running our method. Ours (C), Ours (C&D): Our inference time outputs for a model that was trained only on cats or on cats and dogs respectively. Ours (C)+BA, Ours (C&D)+BA: The outputs of the model trained only on cats or on cats and dogs respectively, after further applying short BA refinement. The numbers for [21], [43] and [64] were obtained from [64].

## References

- Agarwal, S., Furukawa, Y., Snavely, N., Simon, I., Curless, B., Seitz, S.M., Szeliski, R.: Building rome in a day. Communications of the ACM **54**(10), 105–112 (2011) [4](#)
- Agarwal, S., Mierle, K., Team, T.C.S.: Ceres Solver (10 2023), <https://github.com/ceres-solver/ceres-solver> [18](#)
- Akhter, I., Sheikh, Y., Khan, S., Kanade, T.: Nonrigid structure from motion in trajectory space. Advances in neural information processing systems **21** (2008) [3, 7](#)
- Birkl, R., Wofk, D., Müller, M.: Midas v3.1 – a model zoo for robust monocular relative depth estimation. arXiv preprint arXiv:2307.14460 (2023) [11, 19](#)
- Bloesch, M., Czarnowski, J., Clark, R., Leutenegger, S., Davison, A.J.: Codeslam—learning a compact, optimisable representation for dense visual slam.

- In: Proceedings of the IEEE conference on computer vision and pattern recognition. pp. 2560–2568 (2018) [5](#)
6. Bregler, C., Hertzmann, A., Biermann, H.: Recovering non-rigid 3d shape from image streams. In: Proceedings IEEE Conference on Computer Vision and Pattern Recognition. CVPR 2000 (Cat. No. PR00662). vol. 2, pp. 690–696. IEEE (2000) [2](#), [3](#), [7](#)
  7. Bronstein, M.M., Bruna, J., Cohen, T., Velicković, P.: Geometric deep learning: Grids, groups, graphs, geodesics, and gauges. arXiv preprint arXiv:2104.13478 (2021) [3](#)
  8. Brynte, L., Iglesias, J.P., Olsson, C., Kahl, F.: Learning structure-from-motion with graph attention networks. arXiv preprint arXiv:2308.15984 (2023) [4](#)
  9. Butler, D.J., Wulff, J., Stanley, G.B., Black, M.J.: A naturalistic open source movie for optical flow evaluation. In: A. Fitzgibbon et al. (Eds.) (ed.) European Conf. on Computer Vision (ECCV). pp. 611–625. Part IV, LNCS 7577, Springer-Verlag (Oct 2012) [15](#)
  10. Cui, Z., Tan, P.: Global structure-from-motion by similarity averaging. In: Proceedings of the IEEE International Conference on Computer Vision. pp. 864–872 (2015) [4](#)
  11. Dai, Y., Li, H., He, M.: A simple prior-free method for non-rigid structure-from-motion factorization. *International Journal of Computer Vision* **107**, 101–122 (2014) [2](#)
  12. Doersch, C., Yang, Y., Vecerik, M., Gokay, D., Gupta, A., Aytar, Y., Carreira, J., Zisserman, A.: Tapir: Tracking any point with per-frame initialization and temporal refinement. arXiv preprint arXiv:2306.08637 (2023) [3](#)
  13. Eigen, D., Puhrsch, C., Fergus, R.: Depth map prediction from a single image using a multi-scale deep network. *Advances in neural information processing systems* **27** (2014) [12](#)
  14. Engel, J., Koltun, V., Cremers, D.: Direct sparse odometry. *IEEE transactions on pattern analysis and machine intelligence* **40**(3), 611–625 (2017) [4](#)
  15. Engel, J., Schöps, T., Cremers, D.: Lsd-slam: Large-scale direct monocular slam. In: European conference on computer vision. pp. 834–849. Springer (2014) [4](#)
  16. Gao, C., Saraf, A., Kopf, J., Huang, J.B.: Dynamic view synthesis from dynamic monocular video. In: Proceedings of the IEEE/CVF International Conference on Computer Vision. pp. 5712–5721 (2021) [5](#)
  17. Hartley, R., Zisserman, A.: Multiple view geometry in computer vision. Cambridge university press (2003) [1](#)
  18. Karaev, N., Rocco, I., Graham, B., Neverova, N., Vedaldi, A., Ruppel, C.: Cotracker: It is better to track together. arXiv preprint arXiv:2307.07635 (2023) [3](#), [10](#), [12](#), [13](#), [14](#), [17](#)
  19. Kasten, Y., Geifman, A., Galun, M., Basri, R.: Algebraic characterization of essential matrices and their averaging in multiview settings. In: Proceedings of the IEEE/CVF International Conference on Computer Vision. pp. 5895–5903 (2019) [4](#)
  20. Kingma, D.P., Ba, J.: Adam: A method for stochastic optimization. arXiv preprint arXiv:1412.6980 (2014) [10](#)
  21. Kopf, J., Rong, X., Huang, J.B.: Robust consistent video depth estimation. In: Proceedings of the IEEE/CVF Conference on Computer Vision and Pattern Recognition. pp. 1611–1621 (2021) [1](#), [2](#), [5](#), [10](#), [11](#), [19](#), [22](#), [23](#)
  22. Kumar, S., Van Gool, L.: Organic priors in non-rigid structure from motion. In: European Conference on Computer Vision. pp. 71–88. Springer (2022) [2](#)



23. Li, Z., Niklaus, S., Snavely, N., Wang, O.: Neural scene flow fields for space-time view synthesis of dynamic scenes. In: Proceedings of the IEEE/CVF Conference on Computer Vision and Pattern Recognition. pp. 6498–6508 (2021) [2](#)
24. Liu, Y.L., Gao, C., Meuleman, A., Tseng, H.Y., Saraf, A., Kim, C., Chuang, Y.Y., Kopf, J., Huang, J.B.: Robust dynamic radiance fields. In: Proceedings of the IEEE/CVF Conference on Computer Vision and Pattern Recognition. pp. 13–23 (2023) [2](#), [5](#)
25. Loper, M., Mahmood, N., Romero, J., Pons-Moll, G., Black, M.J.: Smpl: A skinned multi-person linear model. In: Seminal Graphics Papers: Pushing the Boundaries, Volume 2, pp. 851–866 (2023) [3](#)
26. Luo, X., Huang, J.B., Szeliski, R., Matzen, K., Kopf, J.: Consistent video depth estimation. *ACM Transactions on Graphics (ToG)* **39**(4), 71–1 (2020) [2](#), [5](#)
27. Maron, H., Litany, O., Chechik, G., Fetaya, E.: On learning sets of symmetric elements. In: International conference on machine learning. pp. 6734–6744. PMLR (2020) [3](#), [7](#), [8](#), [14](#)
28. Mildenhall, B., Srinivasan, P.P., Tancik, M., Barron, J.T., Ramamoorthi, R., Ng, R.: Nerf: Representing scenes as neural radiance fields for view synthesis. *Communications of the ACM* **65**(1), 99–106 (2021) [2](#), [17](#)
29. Moran, D., Koslowsky, H., Kasten, Y., Maron, H., Galun, M., Basri, R.: Deep permutation equivariant structure from motion. In: Proceedings of the IEEE/CVF International Conference on Computer Vision. pp. 5976–5986 (2021) [4](#), [8](#), [9](#), [14](#), [18](#)
30. Mur-Artal, R., Montiel, J.M.M., Tardos, J.D.: Orb-slam: a versatile and accurate monocular slam system. *IEEE transactions on robotics* **31**(5), 1147–1163 (2015) [1](#), [4](#)
31. Newcombe, R.A., Lovegrove, S.J., Davison, A.J.: Dtam: Dense tracking and mapping in real-time. In: 2011 international conference on computer vision. pp. 2320–2327. IEEE (2011) [4](#)
32. Ozyesil, O., Singer, A.: Robust camera location estimation by convex programming. In: Proceedings of the IEEE Conference on Computer Vision and Pattern Recognition. pp. 2674–2683 (2015) [4](#)
33. Park, K., Sinha, U., Barron, J.T., Bouaziz, S., Goldman, D.B., Seitz, S.M., Martin-Brualla, R.: Nerfies: Deformable neural radiance fields. In: Proceedings of the IEEE/CVF International Conference on Computer Vision. pp. 5865–5874 (2021) [2](#)
34. Ranftl, R., Bochkovskiy, A., Koltun, V.: Vision transformers for dense prediction. *ICCV* (2021) [2](#), [5](#)
35. Ranftl, R., Lasinger, K., Hafner, D., Schindler, K., Koltun, V.: Towards robust monocular depth estimation: Mixing datasets for zero-shot cross-dataset transfer. *IEEE Transactions on Pattern Analysis and Machine Intelligence* **44**(3) (2022) [5](#)
36. Saito, S., Huang, Z., Natsume, R., Morishima, S., Kanazawa, A., Li, H.: Pifu: Pixel-aligned implicit function for high-resolution clothed human digitization. In: Proceedings of the IEEE/CVF international conference on computer vision. pp. 2304–2314 (2019) [3](#)
37. Schonberger, J.L., Frahm, J.M.: Structure-from-motion revisited. In: Proceedings of the IEEE conference on computer vision and pattern recognition. pp. 4104–4113 (2016) [1](#), [4](#), [12](#)
38. Sinha, S., Shapovalov, R., Reizenstein, J., Rocco, I., Neverova, N., Vedaldi, A., Novotny, D.: Common pets in 3d: Dynamic new-view synthesis of real-life deformable categories. In: Proceedings of the IEEE/CVF Conference on Computer Vision and Pattern Recognition. pp. 4881–4891 (2023) [3](#), [5](#), [10](#)

39. Sturm, P., Triggs, B.: A factorization based algorithm for multi-image projective structure and motion. In: *Computer Vision—ECCV’96: 4th European Conference on Computer Vision* Cambridge, UK, April 15–18, 1996 Proceedings Volume II 4. pp. 709–720. Springer (1996) [4](#)
40. Tang, C., Tan, P.: Ba-net: Dense bundle adjustment network. arXiv preprint arXiv:1806.04807 (2018) [4](#)
41. Teed, Z., Deng, J.: Deepv2d: Video to depth with differentiable structure from motion. arXiv preprint arXiv:1812.04605 (2018) [5](#)
42. Teed, Z., Deng, J.: Raft: Recurrent all-pairs field transforms for optical flow. In: *Computer Vision—ECCV 2020: 16th European Conference, Glasgow, UK, August 23–28, 2020, Proceedings, Part II* 16. pp. 402–419. Springer (2020) [5](#)
43. Teed, Z., Deng, J.: Droid-slam: Deep visual slam for monocular, stereo, and rgb-d cameras. *Advances in neural information processing systems* **34**, 16558–16569 (2021) [5](#), [10](#), [22](#), [23](#)
44. Tomasi, C., Kanade, T.: Shape and motion from image streams under orthography: a factorization method. *International journal of computer vision* **9**, 137–154 (1992) [4](#)
45. Triggs, B., McLauchlan, P.F., Hartley, R.I., Fitzgibbon, A.W.: Bundle adjustment—a modern synthesis. In: *Vision Algorithms: Theory and Practice: International Workshop on Vision Algorithms Corfu, Greece, September 21–22, 1999 Proceedings*. pp. 298–372. Springer (2000) [4](#)
46. Vaswani, A., Shazeer, N., Parmar, N., Uszkoreit, J., Jones, L., Gomez, A.N., Kaiser, Ł., Polosukhin, I.: Attention is all you need. *Advances in neural information processing systems* **30** (2017) [8](#), [16](#), [17](#)
47. Wang, J., Karaev, N., Ruppel, C., Novotny, D.: Visual geometry grounded deep structure from motion. arXiv preprint arXiv:2312.04563 (2023) [4](#)
48. Wang, J., Ruppel, C., Novotny, D.: Posediffusion: Solving pose estimation via diffusion-aided bundle adjustment. In: *Proceedings of the IEEE/CVF International Conference on Computer Vision*. pp. 9773–9783 (2023) [4](#)
49. Wang, P., Liu, L., Liu, Y., Theobalt, C., Komura, T., Wang, W.: Neus: Learning neural implicit surfaces by volume rendering for multi-view reconstruction. arXiv preprint arXiv:2106.10689 (2021) [2](#)
50. Wang, W., Hu, Y., Scherer, S.: Tartanvo: A generalizable learning-based vo. In: *Conference on Robot Learning*. pp. 1761–1772. PMLR (2021) [5](#)
51. Wang, X., Xiao, T., Kasten, Y.: A hybrid global structure from motion method for synchronously estimating global rotations and global translations. *ISPRS journal of photogrammetry and remote sensing* **174**, 35–55 (2021) [4](#)
52. Wilson, K., Snavely, N.: Robust global translations with 1dsfm. In: *Computer Vision—ECCV 2014: 13th European Conference, Zurich, Switzerland, September 6–12, 2014, Proceedings, Part III* 13. pp. 61–75. Springer (2014) [4](#)
53. Wu, C.: Towards linear-time incremental structure from motion. In: *2013 International Conference on 3D Vision-3DV 2013*. pp. 127–134. IEEE (2013) [1](#), [4](#)
54. Xian, W., Huang, J.B., Kopf, J., Kim, C.: Space-time neural irradiance fields for free-viewpoint video. In: *Proceedings of the IEEE/CVF Conference on Computer Vision and Pattern Recognition*. pp. 9421–9431 (2021) [5](#)
55. Xiu, Y., Yang, J., Tzionas, D., Black, M.J.: Icon: Implicit clothed humans obtained from normals. In: *2022 IEEE/CVF Conference on Computer Vision and Pattern Recognition (CVPR)*. pp. 13286–13296. IEEE (2022) [3](#)
56. Yang, G., Sun, D., Jampani, V., Vlasic, D., Cole, F., Chang, H., Ramanan, D., Freeman, W.T., Liu, C.: Lasr: Learning articulated shape reconstruction from a

- monocular video. In: Proceedings of the IEEE/CVF Conference on Computer Vision and Pattern Recognition. pp. 15980–15989 (2021) [5](#)
57. Yang, G., Sun, D., Jampani, V., Vlasic, D., Cole, F., Liu, C., Ramanan, D.: Viser: Video-specific surface embeddings for articulated 3d shape reconstruction. *Advances in Neural Information Processing Systems* **34**, 19326–19338 (2021) [5](#)
  58. Yang, G., Vo, M., Neverova, N., Ramanan, D., Vedaldi, A., Joo, H.: Banmo: Building animatable 3d neural models from many casual videos. In: Proceedings of the IEEE/CVF Conference on Computer Vision and Pattern Recognition. pp. 2863–2873 (2022) [5](#)
  59. Yang, N., Stumberg, L.v., Wang, R., Cremers, D.: D3vo: Deep depth, deep pose and deep uncertainty for monocular visual odometry. In: Proceedings of the IEEE/CVF conference on computer vision and pattern recognition. pp. 1281–1292 (2020) [5](#)
  60. Yariv, L., Gu, J., Kasten, Y., Lipman, Y.: Volume rendering of neural implicit surfaces. *Advances in Neural Information Processing Systems* **34**, 4805–4815 (2021) [2](#)
  61. Zhang, J.Y., Lin, A., Kumar, M., Yang, T.H., Ramanan, D., Tulsiani, S.: Cameras as rays: Pose estimation via ray diffusion. In: International Conference on Learning Representations (ICLR) (2024) [4](#)
  62. Zhang, Z., Cole, F., Li, Z., Rubinstein, M., Snavely, N., Freeman, W.T.: Structure and motion from casual videos. In: European Conference on Computer Vision. pp. 20–37. Springer (2022) [2](#), [5](#), [10](#), [11](#), [12](#), [19](#), [22](#), [23](#)
  63. Zhang, Z., Cole, F., Tucker, R., Freeman, W.T., Dekel, T.: Consistent depth of moving objects in video. *ACM Transactions on Graphics (TOG)* **40**(4), 1–12 (2021) [2](#), [5](#)
  64. Zhao, W., Liu, S., Guo, H., Wang, W., Liu, Y.J.: Particlesfm: Exploiting dense point trajectories for localizing moving cameras in the wild. In: European Conference on Computer Vision. pp. 523–542. Springer (2022) [5](#), [10](#), [15](#), [22](#), [23](#)
  65. Zhao, W., Liu, S., Shu, Y., Liu, Y.J.: Towards better generalization: Joint depth-pose learning without posenet. In: Proceedings of the IEEE/CVF Conference on Computer Vision and Pattern Recognition. pp. 9151–9161 (2020) [5](#)
  66. Zhou, H., Ummenhofer, B., Brox, T.: Deeptam: Deep tracking and mapping. In: Proceedings of the European conference on computer vision (ECCV). pp. 822–838 (2018) [5](#)
  67. Zhou, Y., Barnes, C., Lu, J., Yang, J., Li, H.: On the continuity of rotation representations in neural networks. In: Proceedings of the IEEE/CVF conference on computer vision and pattern recognition. pp. 5745–5753 (2019) [17](#)
  68. Zou, X., Yang, J., Zhang, H., Li, F., Li, L., Wang, J., Wang, L., Gao, J., Lee, Y.J.: Segment everything everywhere all at once. *Advances in Neural Information Processing Systems* **36** (2024) [12](#), [18](#)